A comparative assessment of ASM4 rockfall barrier modelling

R. Boulaud, Cyril Douthe

A comparative assessment of ASM4 rockfall barrier modelling

R. Boulaud[a], C. Douthe[a]

[a] *Laboratoire Navier, Ecole des Ponts Paristech, Univ Gustave Eiffel, CNRS, 6 et 8 avenue Blaise Pascal, Champs-sur-Marne, France*

Abstract

One key element of flexible rockfall barriers is the net which intercepts the block trajectory. The ASM4 ring net is one of the widely spread net technology for medium to high energy impacts. The accurate modelling of its mechanical behaviour has thus been the aim of many research programs, most of which use the discrete elements method and tension members with material non-linearities. This paper proposes hence a comparison of the three main families of models: linear spring models, tensile ring models and flexural ring models. First, homogenisation techniques are used to characterize intrinsic properties at local scale. Then, the question of the experimental identification of these properties is addressed. Afterwards, the relevance of the identified behaviour is investigated through two case studies. The first one consists in a simple hyperbolic paraboloid structure which has a closed form solution involving large displacements. The second one is based on an experiment on a reduced scale barrier with centered impact and extend the comparison to various kind of data and loading cases. The conclusion presents the main results of the various comparisons, it gives insight on the features that each model can capture and provides some guidelines for designers at early stage design.

Keywords: rockfall barrier, ASM4, intrinsic characteristic, dynamic relaxation, structural analysis

1. State-of-art on the modelling of ASM4 ring nets

1.1. The ASM4 ring net

During the second world war, the ASM4 ring nets were used as Anti-Sub-Marines protective fence (and their name comes from this original use). Since then, part of the stocks were reused for the conception of protection structures like flexible rockfall barriers. Because of its low cost and good mechanical properties, this type of net is still one of the most used in this field. Schematically, these structures can be described as follows: a wire net (usually formed by an ASM ring net, but not necessarily) intercepts the rock trajectory. Then, it deforms, sliding along the supporting cables which are attached to the posts or the cliff through dissipating devices or brakes. Because it has a large capacity of deformation, the ring net is a complex object which has been studied for a long time and lead to many models. The elementary pattern of this net is formed by one ring interlaced with its four neighbours (see Figure 1).

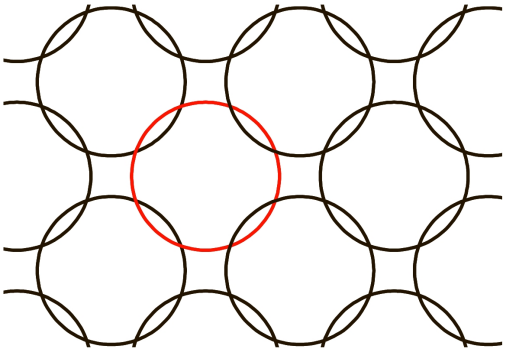

Figure 1: Typical arrangement of rings in ASM4 ring nets where each ring is in contact with four neighbours.

1.2. Review of existing ring models

Even if traditional finite element approaches are sometimes used to accurately simulate rockfall barriers [17,

16], these models often focus on cable nets [7, 20, 21] and double-twisted hexagonal net [1, 33, 25] where sliding within the net are less preponderant. In the case of ASM4, the natural topology of the net and its non-linearities encourage the use of discrete element methods [9, 23, 27, 36, 15]. Among the various discrete models, different strategies have been used to reproduce the typical two stages behaviour of these rings: large deformation by bending during the first stage and then high stiffness due to the axial stiffness of the cable during the second stage. One of the first ASM net model was developed by F. Nicot [27]. He proposed a discrete model in which the rings are represented by a node at their center and interact with each-others by means of an axial spring. This link is described by a non-linear law depending on the elongation of spring. This approach has the advantage of facilitating the geometrical description but the behaviour's determination under any loading condition is complex and needs to fit a multi-linear law. Another disadvantage of this model is that it can only transmit axial forces (in the direction given by the spring) and cannot reproduce any transverse strain orthogonally to the spring strain. This kind of spring model was adopted recently in [15] in a DEM framework as well as FEM in [21, 20]. In its principle, it is similar to the one used for twisted wire net [3, 4, 37, 33].

A few years after F. Nicot's works, H. Grassl proposed a new discrete element model of a ASM4 ring. The shape of his elementary cell is an octagon where one in two vertices represents a contact node between two rings. The eight nodes are connected by truss elements with a variable length. The bending behaviour is conferred by rotational springs on the eight angles [23]. A. Volkwein proposed a simplification of the previous model based on the experimental tensile tests carried out by H. Grassl. He transformed the eight nodes ring by removing the intermediate nodes, keeping only the contact points. Furthermore, he replaced the bending behaviour by the axial strain of two diagonal trusses [35]. By halving the number of degrees of freedom, this geometrical simplification significantly reduces the computation time. Doing so, one breaks the link between the original nature of non linearity (the shape change) and the behaviour of the model, which consequently made the identification of member stiffness less straightforward.

Besides, A. Volkwein' ring model presents some deformation modes with no energy (similarly to hourglass effects in finite elements [18]). Therefore J. Coulibaly used a similar geometry to propose a new model in which links between two consecutive nodes are added to prevent such kinematics [10, 8]. This model also describes very precisely the plastic behaviour of rings, and therefore requires the calibration of many material parameters.

Through out the years, the ASM4 model has thus been enriched toward more accuracy, but also toward larger complexity in the identification process of constitutive parameters which in return makes their use less easy.

1.3. Purpose and methodology of the present study

In this quick literature review, it appears that there are three typical discrete ring models: linear spring models later called model A (after Nicot and following authors), tensile ring models later called model B (after Volkwein and following authors), flexural ring models later called model C(after Grassl and following authors). When fine tuned, all three models show good agreement with experimental results. A structural engineer in early stage design might therefore ask: how do they compared? what features they can capture? and how easy they are to calibrate?

The aim of the present paper is to answer these three questions and to present a comparative assessment of ASM4 models. The proposed methodology is progressive: from local to global behaviour, from small deformation to large rotations.

1.3.1. Identification of intrinsic characteristics with homogeneisation techniques

Comparing these models at net scale may require very often the identification of relevant characteristics at local scale, recalling a continuous description of the net. Some authors have even proposed complete continuous representation of the net. For example N. Sasiharan [32] and S. Dhakal [12] have used both a shell element with a special membrane formulation in a general finite element framework for pocket-type rockfall structures. Recently, A. Mentani *et al.* [24] have also proposed an orthotropic elasto-plastic equivalent membrane model, for a chain-link wire net. Such approaches require the definition of the net local behaviour a priori and thus a knowledge of its intrinsic characteristics.

A first idea for comparing these three typical ASM4 models consists hence in identifying these intrinsic properties by homogeneisation techniques. Such methods are widely used in the field of granular materials or heterogeneous media to identify macroscopic properties [19]. Although often limited to small displacements, this method provides insight on the local behaviour of repetitive structures. A first application to ASM4 ring nets in tension had been made in Ghoussoub [22] and was later completed by the first author [5]. Detailed calculations of closed form solutions being purely technical and somehow standard, they will not be recalled in this paper. However the yet unpublished results will be presented in section 2 and allow for a first comparison of the three models.

1.3.2. Calibration on experimental results from the National Project C2ROP

Discrete like continuous models require the identification of parameters in order to understand how they compared to reality and to be used in a predictive manner. One of the major aim of the C2ROP National Project (www.c2rop.fr) was hence to provide a wide experimental range for the calibration of numerical models that is not limited to standard ETAG test. A working group has formed around the modelling and testing of flexible barriers. A 1:2 scaled barrier was developed with documented separated tests of each components which will be used in section 3 for the calibration of the ring net models at local scale and intrinsic characteristic identification. The results of the quasi-static tests on the complete barrier will then be used in section 5 for the investigation of the influence of the ASM4 model on the global response of the structure in large deformation [29].

The whole set of non-standard experiments realised in this framework has been published in [30]. They show first that there is a significant spreading of results due to the spreading of components characteristics and inherent imperfections induced by on-site rope work. Then, through the comparison of quasi-static and dynamic loading tests on the barrier, they show that qualitatively, on the tested barrier, the two behaviours were very similar. This can be explained by the fact that 85% of the system mass is concentrated in the block which therefore concentrates all the kinetic energy.

1.3.3. Simulation with the dynamic relaxation method

Building on these observations, quasi-static analysis of barriers should be sufficient to evidence the dominant phenomena influencing the net response at reasonable calculation time [see detailed analysis of this hypothesis in 5, chap 5]. Therefore, it was decided to focus on equilibrium configurations which will be investigated by the dynamic relaxation method in the sections 4 and 5. In this method developed by A.S. Day [11], the equilibrium of the system is regarded as the result of a highly damped dynamic process. This simple method has proved very interesting results in structural application and tensile structure [see for example the state-of-art presented by 34].

All numerical computations presented in this paper are thus conducted with a numeric tool developed in laboratory [13, 14, 31]. This tool is implemented in the frame-

work of the commercial software Rhinoceros3D™and more specifically in its plug-in Grasshopper™.

1.3.4. Summary of contributions

The present study proposes thus a comparison of three net models in three steps.

- In Section 2, the intrinsic mechanical properties of the nets formed by the infinite repetition of three discrete models of ASM4 are characterized at **local scale** by an homogenisation method in **small perturbation**.
- Afterwards in Section 3, the stiffness parameters related to the homogenised elasticity tensors are identified thanks to a plane tensile experiment carried out on a square ring net. The experiment being carried out well beyond small perturbations, it provides **local properties** for **small and large displacements**.
- Then, in Section 4, the relevance of the identified membrane behaviours is investigated through the transformation of a square net, initially flat, into a paraboloid hyperbolic shape, a transformation involving smooth **large displacements** with closed form solution **at structural scale**.
- Finally in the last section, the influence of the net model on the **whole rockfall barrier** is investigated through the simulation of an experiment with **full non-linearities**.

2. Identification of ASM4 models intrinsic properties

2.1. Description of the three net models

In this section, the intrinsic mechanical properties of the net, formed by three different discrete models of ASM4 ring net, are identified with help of homogenisation techniques. The considered ring models are strongly inspired by those presented in Section 1.2. The first one (Model A in Figure 2) is an adaptation of the Nicot's model in which each particle is linked to its neighbours by axial springs [26, 15] (in the initial model by Nicot, each ring was connected to six neighbour instead of four in the present paper). The second model (Model B in Figure 2) used the geometry proposed both by A. Volkwein [35] and J. Coulibaly [10]. The four contact points of the ring with its neighbours are connected with a same link. The last one (Model C in Figure 2) is an adaptation proposed by the authors of the model initially developed by H. Grassl [23]. The geometry of the ring is approached by an octagon which is not regular. The eight edges have the same length, the sum of which corresponds to the perimeter of the real ring. The angles formed by two consecutive edges are however not equal. The eight vertices are connected by a strain energy associated to the perimeter of the ring and by a bending energy associated to the local curvature variations [13]. Figure 2 shows the geometry and the interactions of each discrete ring model. The blue squares represent the elementary cells boundary which form the whole net by periodic repetition. For simplicity reasons, the models will be called A, B and C respectively in the rest of the paper.

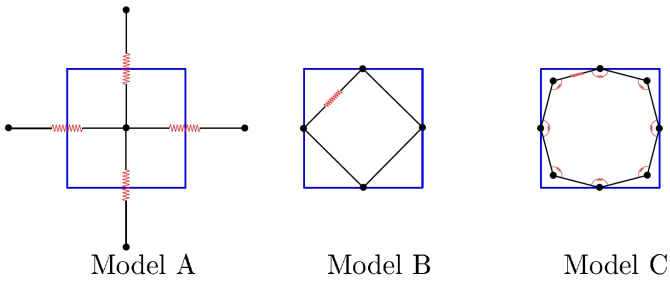

Figure 2: Patterns of the three elementary cells : A. Truss model, B. Tensile ring, C. Bent ring

2.2. Presentation of the homogenisation method

The homogenisation, sometimes also called the asymptotic analysis, includes a set of methods enabling the evaluation of the influence of the micro-structure on the whole medium behaviour. The method presented in this section

has been developed by C. Florence and K. Sab [19]. This method enables the identification of the mechanical properties of an infinite periodic lattice from the resolution of an auxiliary problem of an elementary cell in the framework of the linear elasticity. There are two ways to solve this elementary problem. The first one consists in enforcing a kinematic admissible strain field to the elementary cell. This method is called "kinematic method". The second one consists in enforcing a statically admissible field and is called "static method". Only the kinematic method is presented here and used in this paper for conciseness. It can however be proved that these two methods are dual and give equivalent results [19].

To respect the framework of this method, it is assumed that the ASM4 ring net is a periodic and infinite lattice. This assumption is very strong and will fail when the solution of the problem will be dominated by boundary effects. The elementary cell, whose periodic repetition forms the whole media, is composed of a set of particles of different types (two different particles have the same type if they have an identical neighbourhood: same connectivity, same geometry and same spring characteristics and orientations). Figure 3 shows the formation of the Model C lattice by periodic repetition of its elementary cell: all the particles drawn in red are of the same type (the particles in the other corner points have different spring orientations and, by there, are of different type with different periodic displacements). The purpose of this method is to identify the local strain field and the elastic strain energy of an elementary cell. The effective local field is the one which minimises the elastic energy of the cell. This minimum corresponds to the strain energy in the homogeneous material.

Let $\underline{\underline{E}}$ be the symmetric second order tensor of the global strain, i the index of a particle belonging to the elementary cell and $\underline{X}_i$ its position vector. A kinetic displacement of the particle i is obtained by superposing its linear homogeneous displacement $\underline{\underline{E}} \cdot \underline{X}_i$ and its periodic

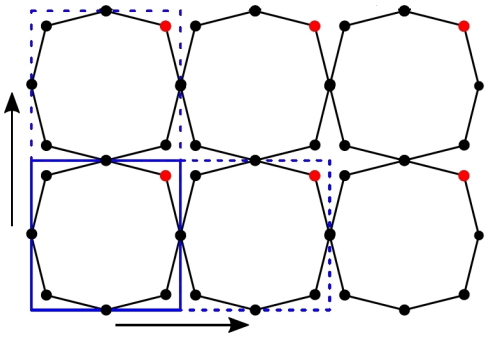

Figure 3: Periodic repetition of Model C elementary cell

displacement $\underline{u}_i^{per}$. Two particles of the same type have also the same periodic displacement. Considering the previous notations, the displacement of the particle i is hence given by: $\underline{u}_i = \underline{\underline{E}} \cdot \underline{X}_i + \underline{u}_i^{per}$. Noting that the particles don't have degrees of freedom in rotation, the set of the kinematic admissible displacement fields $K.A.(\underline{\underline{E}})$ is hence defined by:

$$K.A.(\underline{\underline{E}}) = \{\underline{u} / \underline{u}_i = \underline{\underline{E}} \cdot \underline{X}_i + \underline{u}_i^{per} \quad \forall i \in \text{cell}\} \qquad (1)$$

Then, the elastic strain energy of the discrete elementary cell $\psi^{hom}(\underline{\underline{E}})$ is computed as the sum of the elastic strain energies provided by the interactions between particles in the cell $\psi_i(\underline{u})$ divided by its area A_Ω. The relation of homogenization is thus given by:

$$\psi^{hom}(\underline{\underline{E}}) = \frac{1}{2}\underline{\underline{E}} : \underline{\underline{\underline{\underline{A}}}} : \underline{\underline{E}} = \min_{\underline{u} \in K.A.(\underline{\underline{E}})} \frac{1}{A_\Omega} \sum_i \psi_i(\underline{u}) \qquad (2)$$

where $\underline{\underline{\underline{\underline{A}}}}$ is the overall elasticity tensor. A part of the cell deformation is fixed by the global behaviour of the lattice $\underline{\underline{E}}$. The other part, associated with $\underline{u}^{per}$, requires solving a minimization problem which is quadratic in $\underline{u}^{per}$.

In order to simplify the writing in the further developments, the Voigt's Notation is introduced as in [22]:

$$\underline{\underline{\underline{\underline{A}}}} : \underline{\underline{E}} = \begin{bmatrix} A_{1111} & A_{1122} & A_{1112} \\ A_{2211} & A_{2222} & A_{2212} \\ A_{1112} & A_{2212} & A_{1212} \end{bmatrix} : \begin{bmatrix} E_{11} \\ E_{22} \\ 2E_{12} \end{bmatrix} \qquad (3)$$

2.3. Calculation of the elastic strain energy

The purpose of this section is to describe the different interactions between particles used in the three considered

models of net. Three types of interaction are studied: a spring interaction between a couple of particles, a tensile ring interaction involving a closed set of particles and a flexural beam interaction between three particles (see Figure 4). The first type is used in the three models, the second reflects coupling between strain in orthogonal directions and is used in Model B and C. The third one is only used in Model C. It is important to remember that, in this section, all interactions are elastic, and that all vertices motions are assumed small compared to the characteristic size of the elementary cell.

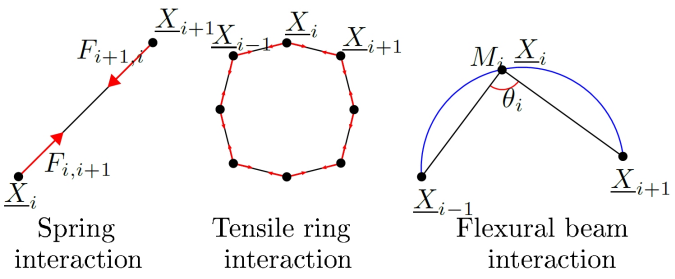

Figure 4: Illustration of the three types of interaction: spring, ring and beam interactions. Note that for the ring interaction, the main characteristic is the loop. The number of nodes in the loop might vary: it is of 8 in model C and 4 in model B.

2.3.1. Bar interaction

The bar interaction simply refers to the spring interaction between a couple of particles. The associated elastic strain energy is thus given, for small strains, by the following expression:

$$\psi_{ba}(\epsilon_{ba}) = \frac{1}{2}\frac{E_{ba}S_{ba}}{l_{ba}}d_{ba}^2 \tag{4}$$

where $\frac{E_{ba}S_{ba}}{l_{ba}}$ is homogeneous to a stiffness in $N.m^{-1}$ and l_{ba} and $\underline{d}_{ba}$ are the rest length (the distance between the two particles in the stress free configuration) and the relative displacement of the interacting particles. This relative displacement is defined by $\underline{d}_i = \underline{u}_{i+1} - \underline{u}_i$. Introducing the particle displacements induced by the global strain, the relative displacement of the couple c_i can be rewritten as:

$$\underline{d}_i = \underline{\underline{E}} \cdot \underline{l}_i + \Delta\underline{u}_i^{per} \quad \text{with} \quad \underline{l}_i = \underline{X}_{i+1} - \underline{X}_i \tag{5}$$

2.3.2. Ring interaction

The second interaction is of ring type. It refers to an ordered set of N particles. Ordered means that each particle has always the two same neighbours. In other words, each particle belongs to two consecutive couples of particles and the ring interaction acts on the ordered series of these N couples (for instance in Figure 4 the particle i belongs to the couples $[i-1, i]$ and $[i, i+1]$). The form of the elastic strain energy related to the ring interaction is the same as the one used in the case of the bar interaction:

$$\psi_r(\epsilon_r) = \frac{1}{2}\frac{E_r S_r}{l_r}d_r^2 \tag{6}$$

The ring elongation is the sum of the elongations of each couple c_i:

$$d_r = \sum_{k=1}^{N} d_i \tag{7}$$

As previously, the expression of the overall rest length is also derived from the rest length of each couple by:

$$l_r = \sum_{k=1}^{N} l_i \tag{8}$$

2.3.3. Bending interaction

Experimental results on ring tensile tests have shown a stage of the behaviour which is due to the ring bending (see Figure 7). To model it with only the assumptions of the cable theory, many authors have chosen to add material non-linearities to reproduce the stiffness changes [27, 36, 10, 15]. However, there exist simple models to reproduce bending forces in axi-symmetric sections [2, 13, 14, 31]. These models have the advantage of not requiring rotational degrees of freedom to compute the bending moment. An elastic energy depending only on the nodal translation can thus be associated with this bending interaction. In standard strength of material, the bending moment is computed by:

$$\|\underline{M}_i\| = \frac{EI}{r_i} \tag{9}$$

where r_i is the local radius of curvature associated with the particle i and calculated from the osculating circle passing

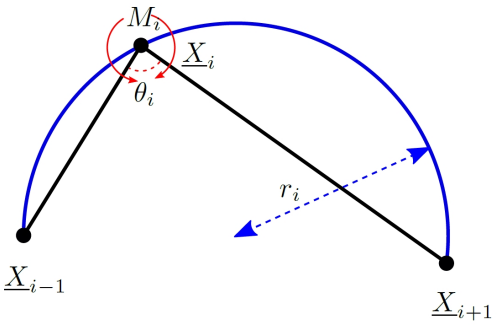

Figure 5: Calculation of the radius of curvature and of the bending moment

through the particles $(i-1, i, i+1)$ (see right of Figure 4). Using the same notations as in section 2.3.1, the radius of curvature is defined by:

$$r_i = \frac{\|\underline{l}_{i-1,i+1} + \underline{d}_{i-1,i+1}\|}{2\sin\theta_i} \tag{10}$$

where θ_i is the angle formed by the vectors $(\underline{l}_{i-1} + \underline{d}_{i-1})$ and $(\underline{l}_i + \underline{d}_i)$.

In the framework of the proposed homogenization method, energies are quadratic functions of the strain field. To this end, the sine function must be expressed as a function of the particle couple :

$$\sin\theta_i \cdot \underline{e_z} = \frac{(\underline{l}_{i-1} + \underline{d}_{i-1}) \wedge (\underline{l}_i + \underline{d}_i)}{\|\underline{l}_{i-1} + \underline{d}_{i-1}\|\|\underline{l}_i + \underline{d}_i\|} \tag{11}$$

In the case of the ring, the initial curvature is not equal to zero. The calculation of the bending moment must be thus slightly modified to account for the curvature variation:

$$\begin{aligned}\frac{\underline{M}_i}{2EI} =& \frac{(\underline{l}_{i-1} + \underline{d}_{i-1}) \wedge (\underline{l}_i + \underline{d}_i)}{\|\underline{l}_{i-1} + \underline{d}_{i-1}\|\|\underline{l}_i + \underline{d}_i\|\|\underline{l}_{i-1,i+1} + \underline{d}_{i-1,i+1}\|} \\ &- \frac{\underline{l}_{i-1} \wedge \underline{l}_i}{\|\underline{l}_{i-1}\|\|\underline{l}_i\|\|\underline{l}_{i-1,i+1}\|}\end{aligned} \tag{12}$$

Expression (12) is used in this form for the implementation in the custom code cited in Section 1.3.3. To simplify notations, the variables referring to the couple of particles $(i-1, i+1)$ will be indexed in the rest of the paper with the subscript i and the superscript c (for chord). To remain within the framework of the homogenisation method [19], the particle displacements must remain small and the expression of the bending moment (12) can hence be linearised according to the relative displacements of each couple of particles: $\underline{d}_{i-1}$, $\underline{d}_i$ and $\underline{d}_{i-1,i+1} = \underline{d}_i^c$.

$$\begin{aligned}\frac{\underline{M}_i}{2EI}\|\underline{l}_{i-1}\|\|\underline{l}_i\|\|\underline{l}_i^c\| =& \underline{l}_{i-1} \wedge \underline{d}_i + \underline{d}_{i-1} \wedge \underline{l}_i \\ &+ \underline{l}_i \wedge \underline{l}_{i-1}\left(\frac{\underline{l}_i^c \cdot \underline{d}_i^c}{\|\underline{l}_i^c\|^2} + \frac{\underline{l}_{i-1} \cdot \underline{d}_{i-1}}{\|\underline{l}_{i-1}\|^2} + \frac{\underline{l}_i \cdot \underline{d}_i}{\|\underline{l}_i\|^2}\right)\end{aligned} \tag{13}$$

The elastic bending energy associated with the particle i is then given by the formula:

$$\psi_{be}^i = \frac{1}{2}\frac{\underline{M}_i{}^2}{EI}\frac{\|\underline{l}_{i-1}\| + \|\underline{l}_i\|}{2} \tag{14}$$

Even if in this section, the elementary cells are considered planar, it can be remarked that the expressions of the bending moment and of the elastic bending energy presented above ((12) (14)) remain valid for the study of 3D problems [13].

These three interactions enable the calculation of the strain energy of each elementary cell introduced in Section 2.1. It can be reminded that in Figure 2, the cell perimeters are limited by the square drawn in blue. Only Model C has particles whose displacements do not only depend on the overall strain field $\underline{\underline{E}}$. Therefore, the identification of the homogeneous elasticity tensor requires the resolution of a minimisation problem only in this last case.

2.4. Identification of the stiffness matrices

For this part of the study, it is assumed that the three models consist in infinitely periodic material under uniform strain undergoing small deformation.

2.4.1. Model A

In this model, each ring is represented by one particle in its center and four links of bar-type interaction connecting it with its four neighbours (Model A in Figure 2). The identification of the homogeneous elasticity tensor is straight forward and lead to:

$$\underline{\underline{A}}^A = \begin{pmatrix} K_{ba}^A & 0 \\ 0 & K_{ba}^A \end{pmatrix} \tag{15}$$

with:

$$K_{ba}^{A} = \frac{E_{ba}^{A} S_{ba}^{A}}{2R} \tag{16}$$

where superscript A refers to model A, R is the radius of the ring, which means that $2R$ is here the length between two neighbour particles and $E_{ba}^{A} S_{ba}^{A}$ is the stiffness of the bar interaction in N. The equivalent homogeneous net has no shear stiffness and a null Poisson's ratio.

2.4.2. Model B

In this model, each ring is formed by four particles located at the contact points with the adjacent rings (see Figure 1). The loads are transmitted between the particles through only one ring interaction. Using the relation (6) and (2), the derivation of the stiffness matrix is straightforward again and leads:

$$\underline{\underline{A}}^{B} = \frac{\sqrt{2}}{2} \begin{pmatrix} K_r^B & K_r^B \\ K_r^B & K_r^B \end{pmatrix} \tag{17}$$

with:

$$K_r^B = \frac{E_r^B S_r^B}{2R} \tag{18}$$

where superscript B refers to model B, R is the ring radius and K_r^B is the stiffness of the ring perimeter. In Model B the shear stiffness is still zero, but the Poisson ratio is now equal to 1 which introduces a significant difference with Model A in which stresses in orthogonal directions were uncoupled.

2.4.3. Model C

Unlike the two previous elementary cells, Model C has inner nodes which do not belong to the boundary of the cell and whose displacements are not determined by periodicity conditions as in Model A (see Figure 3). The elastic energy expression thus depends on the periodic displacements of the inner nodes. The identification of the elasticity tensor is, this time, a little more complex and requires solving an auxiliary minimisation problem. The detail of the calculations is proposed in Boulaud's Phd thesis [5]. It is proved that the elasticity tensor of Model C can be numerically expressed as:

$$\underline{\underline{A}}^{C} = 2.3 K_{be}^{C} \begin{pmatrix} 1 & 0.8 & 0 \\ 0.8 & 1 & 0 \\ 0 & 0 & 0.4 \end{pmatrix} \tag{19}$$

where superscript C refers to model C and

$$K_{be}^{C} \sim \frac{E^C I^C}{R^3} \tag{20}$$

K_C is homogeneous to a flexural stiffness with I^C the inertia of the ring.

2.5. Comparison of the elasticity tensors of the three models

The three models have been presented by order of complexity. The Model A composed of two bar interactions has a null Poisson ratio and no shear stiffness. A ring interaction is added in Model B and its Poisson ratio is now equal to 1 but the cell has still no shear stiffness. This Poisson ratio equal to 1 corresponds to a kind of plane strain incompressibility condition which reflects an important physical property of ASM4 rings. Furthermore the introduction of a bending stiffness in Model C has slightly lowered the Poisson ratio to 0.79 and conferred shear stiffness to the net.

The comparison of the intrinsic elastic properties of these three models indicates thus, that, for small strains, the way they transfer loads is different. The micro-structure of Model C being closer to the real ring structure, it is expected that its behaviour is closer to the reality. Nonetheless, it will be shown in the next section that, when trying to identify the characteristic stiffnesses of the three models, Model C is also the simplest.

3. Identification of the intrinsic equivalent behaviour through a large deformation tensile test

3.1. Experimental set-up

The experiment presented below, carried out in the framework of the french national project "C2ROP" [28,

30], consists of a square and rigid support frame on which a three by three ASM4 ring net is fixed (see Figure 6). The rings are considered to be perfectly circular in their relaxed geometry with a radius $R_0 = 13.5$ cm. They are made of 7.5 mm strand of galvanised steel. A uni-axial tensile loading is applied to the ring net by pulling one edge of the support frame. The normal displacement of this edge is imposed while on the other edges tangential displacements are free and normal displacements are blocked. Force sensors are placed on the moving edge and on one of the lateral edges so that the whole resultant forces applied by the net on the frame are recorded. Considering then that the deformation in the net is uniform, the force applied on a single ring is assumed to be equal to one third of the total force applied on the edge.

Furthermore, the order of magnitude of displacements applied in this test was chosen in order to investigate also a deformation range beyond that of previous section. Equivalent material characteristics identified by this test will thus cover the domain of small perturbations (for strains smaller than 4% of the specimen size) and also allow for the identification of a second linear domain (for strains larger than 25%) where the rings have become diamonds and work in pure tension. The choice was made to identify only two parameters for each model to ease comparisons: one for small strains (and bending energy in the ring), one for large strains(and strain energy in the ring). Other choices with more parameters could also be made, like in [10]).

3.2. Model A

In Model A, the non-linear behaviour of the ring is modelled by means of material non-linearity. It is assumed that the tensile behaviour of the ring can be described by means of a bi-linear law in traction with a null stiffness in compression (similarly to what is made by F. Nicot *et al* [27] or by L. Dugelas *et al* [15]. The left part of Figure 7 shows the pattern of this model drawn in red as well as

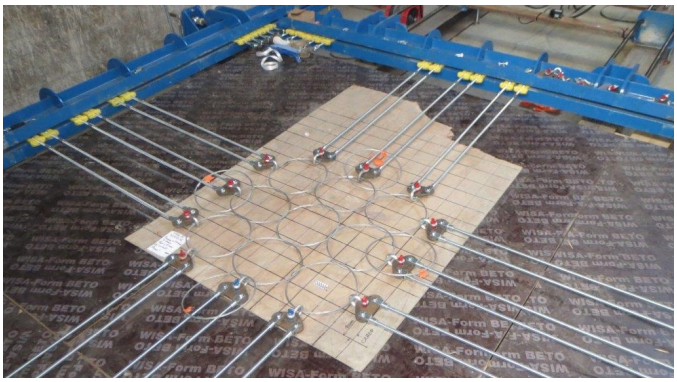

Figure 6: Experimental set-up of the plane tensile test on a ASM4 ring net (by courtesy of national project C2ROP).

the domain of the elementary cell drawn with a dotted line. The identification of the bi-linear behaviour law from the experimental results is presented in the right part of the figure. Referring to the notations of Figure 7 the axial displacements of the moving edge is noted U_a and the axial resultant force F_{axial}. The behaviour is given according to ϵ_a, the axial Green-Lagrange strain applied to the net during the experiment:

$$\epsilon_a = \frac{1}{2}\left[\left(\frac{U_a + 6R_0}{6R_0}\right)^2 - 1\right] \tag{21}$$

The two stiffnesses of the bi-linear behaviour which are noted $K^A_{ba,1}$ and $K^A_{ba,2}$ respectively, are fitted from the experimental results by means of least squares fitting on the two asymptotic behaviours. The low stiffness is fitted for axial strains lower than 4% whereas the second stiffness is fitted for strains higher than 25%. The parameter values are given below. ϵ^A_{lim} is the strain for which the change of stiffness occurs.

$$\begin{cases} K^A_{ba} = 0\,\text{kN.m}^{-1} & \text{if} \quad \epsilon \leq 0 \\ K^A_{ba} = 31\,\text{kN.m}^{-1} & \text{if} \quad \epsilon \leq \epsilon^A_{lim} = 23\% \\ K^A_{ba} = 2160\,\text{kN.m}^{-1} & \text{if} \quad \epsilon > \epsilon^A_{lim} = 23\% \end{cases} \tag{22}$$

3.3. Model B

In Model B, the non-linear behaviour is modelled thanks to one ring with a bi-linear behaviour in traction, in the same way as for the Model A, with a low stiffness for the

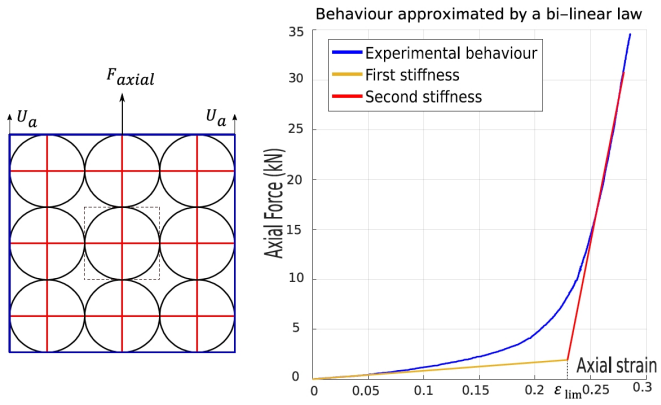

Figure 7: Pattern of Model A and fitting of its bi-linear behaviour

bending stage and a high stiffness for the tensile stage. In this model, initially, the rings have a diamond shape and their perimeter is actually much lower than the perimeter of the physical ring. It is self understandable that the stiffness change in the model will occur when the perimeter of the diamond ring will get close to the perimeter of the circular ring, which corresponds to the fact that, physically, iso-perimetric deformation of the circular ring into a diamond ring is achieved and cables go straight from contact point to contact point. The initial pattern of Model B as well as the calibration of the element's stiffness are presented in Figure 8.

The fitting of the ring's characteristics requires to calculate the strain of the diamond ring from the displacements of the moving edge U_a and its tensile stress from the axial force. The Green-Lagrange strain of the diamond ring, ϵ_r^B, is given by the following expression:

$$\epsilon_r^B = \frac{1}{2}\left(\frac{4R_0^2 + \left(2R_0 + \frac{U_a}{3}\right)^2}{8R_0^2} - 1\right) \tag{23}$$

Referring to the left scheme in Figure 8 the tensile force in the diamond ring is calculated by:

$$N_r^B = \frac{1}{2}\frac{F_{axial}}{3}\frac{\sqrt{4R_0^2 + \left(2R_0 + \frac{U_a}{3}\right)^2}}{2R_0 + \frac{U_a}{3}} \tag{24}$$

The stiffnesses are still calculated by fitting the real behaviour for the same limit of axial strains in model A (lower than 4% and higher than 25% of the specimen length), which correspond to strains of the ring lower than 2% and higher than 12.5%. The parameter of Model B are hence:

$$\begin{cases} K_r^B = 0\,\text{kN.m}^{-1} & \text{if} \quad \epsilon \leq 0 \\ K_r^B = 43\,\text{kN.m}^{-1} & \text{if} \quad \epsilon \leq \epsilon_{lim}^B = 11.5\% \\ K_r^B = 2750\,\text{kN.m}^{-1} & \text{if} \quad \epsilon > \epsilon_{lim}^B = 11.5\% \end{cases} \tag{25}$$

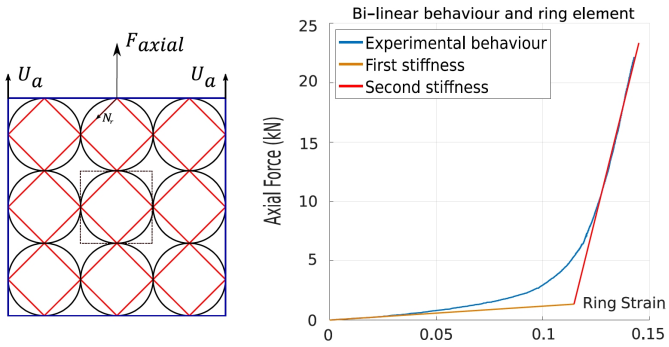

Figure 8: Pattern of Model B and fitting of its behaviour

3.4. Model C

Model C behaviour being richer than the previous ones, the characterization of its mechanical property is directly performed from the expression of the elasticity tensor (19) and refers to the notations used in [5]. For small axial displacements applied during the experiment, the following equation is valid:

$$\frac{F_{axial}}{2R_0} = A_{1111}\epsilon_a = 2.3K_{be}^C\epsilon_a \tag{26}$$

where ϵ_a is still the axial strain. Moreover, in the case of Model A (see section 3.2), it has been already shown that: $\frac{F_{axial}}{2R_0\epsilon_a} = 31\,\text{kN.m}^{-1}$, which enables to straightforward deduce the value of K_{be}^C. Then, for large axial strain, the behaviour of Model C becomes similar to the one of Model B, because the stiffness K_r^C is large compared to K_{be}^C (see [5]), the octagonal ring deform into a diamond shape. To identify the value of the ring stiffness, the same approach as in Section 3.3 can thus used. However, the Green-Lagrange strain needs to be modified by taking into

account the actual perimeter of the octagonal ring:

$$\epsilon_r^C = \frac{1}{2}\left(\frac{4R_0^2 + \left(2R_0 + \frac{U_a}{3}\right)^2}{4\pi^2 R_0^2} - 1\right) \tag{27}$$

The fitting of this last parameter is presented in Figure 9 as well as the pattern of the Model C. Finally, the parameters of the Model C are:

$$K_r^C = 1140\,\text{kN.m}^{-1} \quad \text{and} \quad K_{be}^C = 13\,\text{kN.m}^{-1} \tag{28}$$

Unlike the previous models, this one does not require the identification of a third parameter linked to the material non-linearity. The transition from one behaviour to the other is smoothly done through the geometric deformation of the ring.

For the sake of completeness, it must be added here that an additional geometric constraint has been introduced in model C insuring that the nodes, which do not belong to the cell boundary, move along the bisector of the chord formed by their two neighbour nodes. For numerical computation this geometric constraint is changed to a mechanical constraint by adding eight springs along the edges of the octagonal ring. In order to minimize the influence of these springs on the behaviour of Model C, their stiffness must be very small compared to the stiffness of the ring K_r^C. Computation will hence be performed with a value of $10^{-2}K_r^C$.

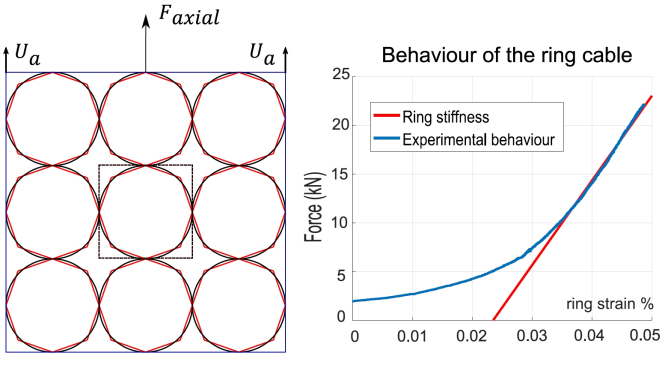

Figure 9: Pattern of Model C and fitting of its behaviour

3.5. Assessment of the homogeneous behaviours

The aim of this section is the validation of the homogeneous behaviour of the three models which have just been characterised. For this purpose, the experiment described in section 3.1 is numerically simulated. All calculations are carried out with a custom DEM code. The evolution of the axial and transverse forces are presented according to the axial displacement for each model in Figure 10.

It is observed that the stiffness parameters identified in the sections 3.2, 3.3 and 3.4 allow to correctly approximate the net behaviour in the traction direction. However as explained in Section 2.5, the model A has a null Poisson ratio and the resultant force is hence null in the transverse direction. Furthermore the model C reproduces more accurately the behaviour of the net, without any material non-linearity, because its micro-structure accounts for the right geometric non-linearity. The geometrical description of the real ring by an octagon also enables to correctly reproduce the behaviour in the transverse direction. It is observed in Figure 10 that the bi-linear law of model B enables to reproduce only the two asymptotic behaviours but is not enough to describe the progressive change of the stiffness. As mentioned earlier, more complex behaviours could be implemented, using for instance polynomial laws as in [10, 6], but that would require the identification of more parameters with difficult physical interpretation.

3.6. Conclusion of the experimental identification process

The plane behaviours of the three net models are now completely characterized and give each one a good approximation of the real net behaviour. The experiment allowed for an identification which goes beyond small perturbations and covers the whole range of uni-axial deformations of the rings in real structures. The mechanical properties, identified in this section for the three models, will be those used in the rest of this paper. At this stage of the comparison, Model C seems to be more relevant to describe accurately the behaviour of a ring net. In a rockfall bar-

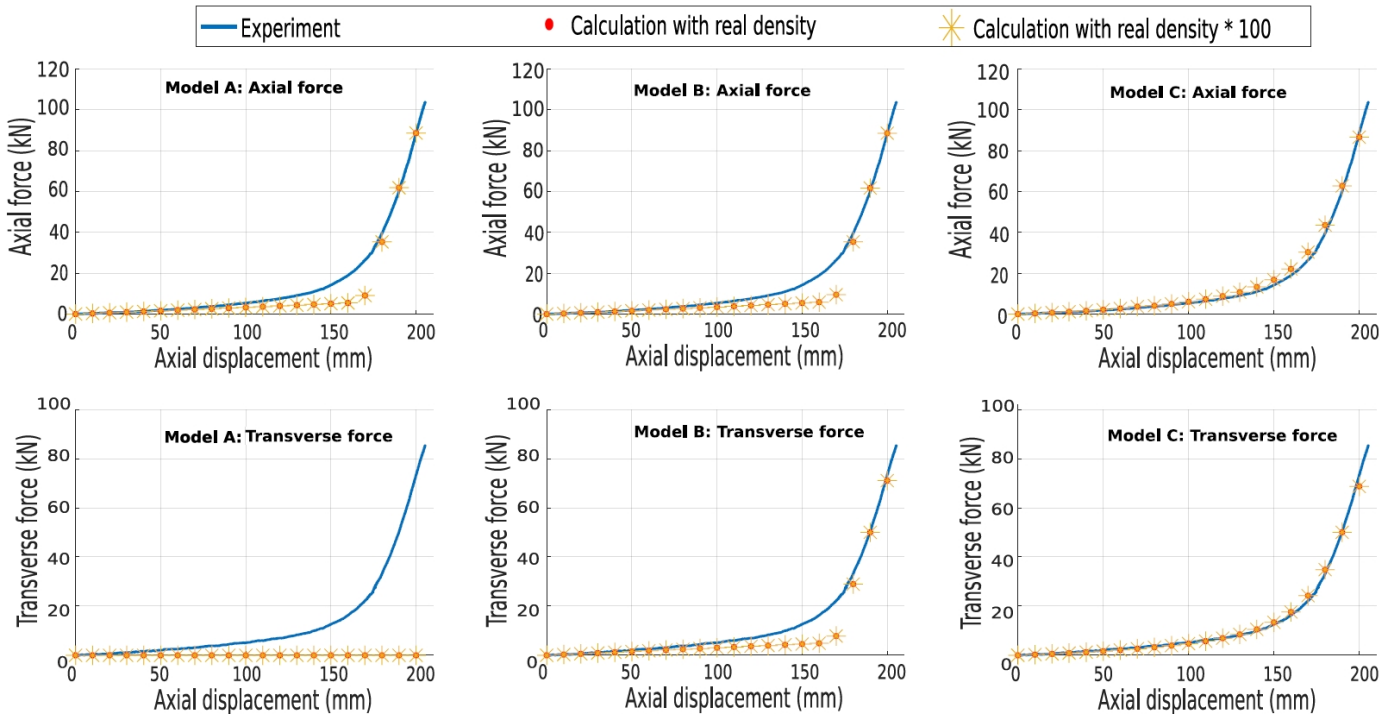

Figure 10: Comparison of the behaviour of the three models (continuous line: experimental results with 3x3 rings specimen; dots and stars: numerical results with real density of rings (3x3) and 100 times density (30x30) respectively).

rier, however, when the net is impacted by a boulder, it undergoes both large out-of-plane displacements and large strains. Before studying the behaviour of the models under these severe conditions, a intermediate loading case, for which closed form solution can be determined, is assessed in the next section. It will give a first indication on how local properties influence results at structural scale.

4. First case-study: structure under large displacements with closed form solution

The case study investigated here consists in the transformation of a flat square membrane in a quasi hyperbolic paraboloid. In this transformation, no external load is applied and only the boundaries of the square are moved vertically proportionally to their distance to the centre of the square. Defining hence the orthonormal coordinate system (x_1, x_2, x_3) and $u_1(x_1, x_2)$, $u_2(x_1, x_2)$ and $u_3(x_1, x_2)$ the displacements in the three directions, the transformation called hypar transformation and presented in Figure 11 is characterised by:

$$u_3(x, y) = \frac{x_1 x_2}{c} \tag{29}$$

Considering that H is the vertical displacement of each corner (see Figure 11), the parameter c is given by: $c = \frac{l^2}{4H}$.

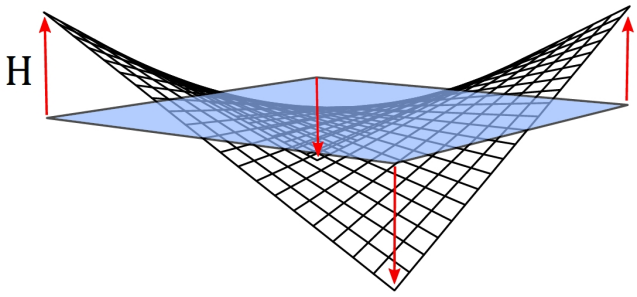

Figure 11: Transformation of the flat membrane in a hyperbolic paraboloid

In the following, the equilibrium state of the membrane under the Von Karman assumptions will be first established, then a convergence study with various mesh den-

sity of the three models will be conducted before a final comparative assessment is presented.

4.1. Equilibrium state of the membrane undergoing an hypar transformation

According to the assumptions of the Von Karman plate theory: large out-of-plane displacements but small plane strains [38], the components of the Green-Lagrange strain (ϵ_{11}, ϵ_{12} and ϵ_{22}) of the equivalent membrane can be deduced from the derivative of displacements in the tangent plane (u_1 and u_2) and the square of the displacement in the normal direction (u_3) by:

$$\begin{aligned} \epsilon_{11} &= u_{1,1} + \tfrac{1}{2}u_{3,1}^2 \\ \epsilon_{22} &= u_{2,2} + \tfrac{1}{2}u_{3,2}^2 \\ \epsilon_{12} &= \tfrac{1}{2}\left[u_{1,2} + u_{2,1} + u_{3,1}^2 u_{3,2}^2\right] \end{aligned} \tag{30}$$

Assuming then a linear elastic behaviour, the constitutive law of the membrane takes the following form:

$$\begin{pmatrix} N_{11} \\ N_{22} \\ N_{12} \end{pmatrix} = \begin{pmatrix} A_{1111} & A_{1122} & 0 \\ A_{1122} & A_{2222} & 0 \\ 0 & 0 & A_{1212} \end{pmatrix} \begin{pmatrix} \epsilon_{11} \\ \epsilon_{22} \\ 2\epsilon_{12} \end{pmatrix} \tag{31}$$

where $N_{11,}$, N_{22} and N_{12} represent the components of membrane forces in the shell and A_{ijkl} the components of the stiffness matrix. For the three equivalent homogeneous membranes, the equivalent stiffness matrix has been identified in (15), (17) and (19). They are all orthotropic with the same stiffness in the two principal directions so that $A_{1111} = A_{2222}$. So, introducing the Poisson ratio ($\nu = \frac{A_{1122}}{A_{1111}}$), two cases have to be distinguished: Membrane A and B where the shear stiffness is zero and Membrane C where the shear stiffness is non zero.

Without external forces and assuming that the bending stiffness is negligible in comparison to the in-plane stiffness, the solution of von Karman's problem [38] can be sought in such a way that $u_3(x_1, x_2) = \frac{x_1 x_2}{c}$ everywhere and reduces hence to:

$$\begin{cases} u_{1,11} + \frac{A_{1122}}{A_{1111}}\left(u_{2,12} + \frac{x_1}{c^2}\right) + \frac{A_{1212}}{A_{1111}}\left(u_{1,22} + u_{2,12} + \frac{x_1}{c^2}\right) = 0 \\ u_{2,22} + \frac{A_{1122}}{A_{2222}}\left(u_{1,12} + \frac{x_2}{c^2}\right) + \frac{A_{1212}}{A_{2222}}\left(u_{1,12} + u_{2,11} + \frac{x_2}{c^2}\right) = 0 \\ A_{1212}\left(u_{1,2} + u_{2,1} + \frac{x_1 x_2}{c^2}\right) = 0 \end{cases} \tag{32}$$

First case: $A_{1212} = 0$. In this case, the in-plane displacements u_1 and u_2 can be expressed each one as a single variable function. The boundary conditions impose that the in-plane displacements are null in the four corners. Moreover the symmetry conditions impose that $u_1(0, x_2) = u_2(x_1, 0) = 0$. Finally it is established that:

$$\begin{cases} u_1(x_1) = \frac{\nu}{6c^2} x_1 \left(\frac{l^2}{4} - x_1^2\right) \\ u_2(x_2) = \frac{\nu}{6c^2} x_2 \left(\frac{l^2}{4} - x_2^2\right) \end{cases} \tag{33}$$

Without shear stiffness, it is possible to find a solution of the problem (32) which satisfies the condition: $u_3(x_1, x_2) = \frac{x_1 x_2}{c}$ by imposing only a vertical motion to the boundary $\partial\Omega$. It can be also noted that in the trivial case for which the Poisson ratio ν is equal to zero, the equilibrium equations are satisfied without in-plane displacements.

Second case: $A_{1212} \neq 0$. This time, the third equation of (32) imposes that the shear strain is null. The displacement field solution is then given by:

$$\begin{cases} u_1(x_1, x_2) = \frac{x_1}{4c^2}\left[\frac{l^2}{4} - x_2^2 + \frac{\nu}{3}\left(\frac{l^2}{4} - x_1^2\right)\right] \\ u_2(x_1, x_2) = \frac{x_2}{4c^2}\left[\frac{l^2}{4} - x_1^2 + \frac{\nu}{3}\left(\frac{l^2}{4} - x_2^2\right)\right] \end{cases} \tag{34}$$

Under this condition, it is hence observed that the in-plane displacements satisfying the conditions: $u_3(x_1, x_2) = \frac{x_1 x_2}{c}$ are maximum in the middle of each edge.

4.2. Behaviour of the net models for an hypar loading

In this section, the three equivalent membranes are loaded in displacement by imposing the conditions provided by (34) to their boundary. This specific shear-free state of strain allows to compare the behaviour of the three models.

4.2.1. Behaviours of the homogeneous equivalent materials

Without shear strain and for small displacements, the differences between the behaviour of the three homogeneous materials are only due to the value of the Poisson ratio (see Section 2.4). From the expression (34) of the displacement field, the strains are calculated using (30) and then the stress field, using (31):

$$\underline{\underline{N}} = \begin{pmatrix} N(x_2) & 0 \\ 0 & N(x_1) \end{pmatrix} \tag{35}$$

with

$$N(x) = \frac{A_{1111}}{4c^2}\left(\frac{l^2(3+\nu)(1+\nu)}{12} + (1-\nu)^2x^2\right) \tag{36}$$

It can be remarked that, for a Poisson ratio equal to 1, which is the case for Model B, the stress state is uniform and isotropic in the equivalent material. The geometry of the membrane is therefore a minimal surface. Otherwise the stress evolves quadratically.

To go further and easily compare analytic and numerical results, the resultant force applied along an edge of the membrane provides an interesting global measure of forces in the membrane, it is given by:

$$F = \int_{-\frac{l}{2}}^{\frac{l}{2}} N(x)\mathrm{d}x = \frac{1+\nu}{3}A_{1111}\frac{4H^2}{l} \tag{37}$$

4.2.2. Numerical behaviour of the net models

The common modelling choice in flexible rockfall barrier is to use one numerical element for one physical element. However, considering the numerical model as a pure discretisation problem of a continuous mechanical problem, it is common knowledge that the size of elements relatively to the characteristic size of the structure has an influence on the quality of the approximated solution given by the numerical model. One might therefore ask if, in the present study, the size of the ring elements is sufficiently small to reproduce the behaviour of the net, especially in this case-study where a closed form solution exists.

To investigate this question a convergence study is thus conducted by varying the size of the ring elements and keeping the size of the hypar structure constant, as well as the net stiffness per unit length. To this end, the individual stiffness of the ring element have to be adjusted for each calculation. Indeed, the size of the ring element appears in all the expressions of the stiffness identified in section 3 (see 16, 18 and 20). To keep the stiffness per unit length constant, it was thus decided to modify the Young Modulus of the ring inversely to R the radius of the ring element for model A and B and to R^3 for model C.

In this convergence study, a 1 m square net is deformed in an hypar form with a ratio $\frac{H}{l}$ equal to $\frac{1}{4}$. The choice of the ratio value is deliberately made here beyond the hypothesis of small displacements. The results are presented in Figure 12. The relative gap between the values obtained for the highest density and the current density is plotted as a function of the mesh count (the number of rings in the net. It can be noticed that for the three models, errors of less than 1 % are achieved for a net of 9x9 rings, which is comparable to the real mesh density in a typical rockfall barrier unit (for example the net shown in Figure 14 has 17×23 rings between two successive posts). With a mesh density of 15×15 rings, the errors falls down to 1.5‰for the models A and B and 2.5‰for Model C.

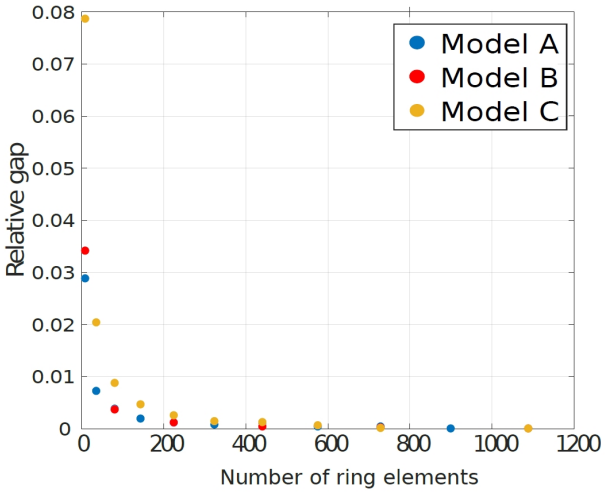

Figure 12: Convergence study in terms of mesh density

Now that the mesh density to be used for numerical simulations has been investigated, the behaviour of the

models can be compared with the one of their equivalent homogeneous membrane on a 9×9 net, which ensures hence less than 1% error. The computations are carried out by varying the ratio $\frac{H}{l}$ and comparing the resultant applied to an edge (37). The results are presented in Figure 13, where closed-form solutions of each model is referred as "analytic" curve and discrete element model as "numerical" curve. It is observed that for the models A and B, the analytic behaviour of the equivalent membrane is very close to the one of the discrete net. The stiffening induced by the geometric changes of the underlying surface (the more Gaussian curvature in the surface, the stiffer the structure) is clearly captured by the models. The influence of the Poisson ratio, predicted by the theoretical expression of the resultant force (37), is also verified for the discrete nets ($F_A \approx 2F_B$).

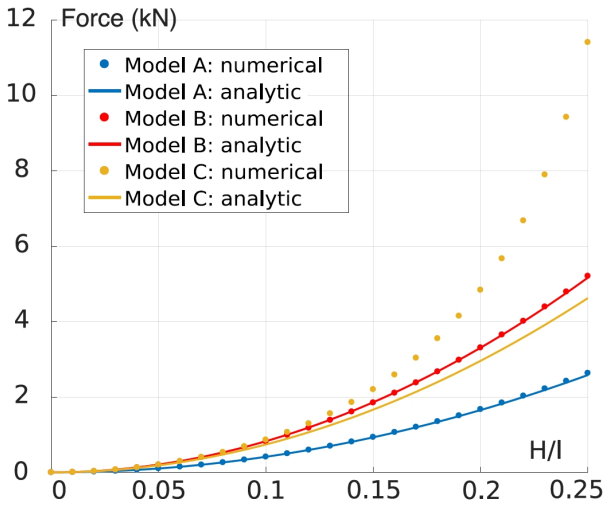

Figure 13: Comparison of the three net models

For model C, the numerical model predicts an additional stiffening which is not included in the closed form solution. This stiffening corresponds to geometrical changes at local scale: the ring geometry varies significantly with the ratio $\frac{H}{l}$ from octagonal shape toward diamond shape. The equivalent homogeneous elastic properties of the membrane increase thus with the deformation and cannot be considered constant. Interestingly, this should also be the case for model B where the ring shape also changes from square to diamond. In the deformation range studied here, the order of magnitude of local stiffness increases induced by these changes in model B are thus one order of magnitude lower than the one induced by changes in model C.

5. Second case-study: complex rockfall barrier under large displacements

The simple academic case study proposed in Section 4 has shown that, at structural scale, the response of the three models have significant differences, even in the global response to simple loading. In this second case-study, a realistic application is chosen with the aim of investigating which features of the behaviour of a rockfall barrier the three models can capture. Large deflections will still be evaluated with the dynamic relaxation method. Numerical results obtained with the three models are first compared to experimental results on a centred impact and then between them on non-centred impacts.

5.1. Experimental set-up

5.1.1. Barrier architecture

A full-scale quasi-static experiment was carried out in the framework of the french national project C2ROP (previously mentioned in Section 3.1) on a rockfall barrier composed of three units, each one 5 meters wide and 2.75 meters high [29, 30, 15]. A picture of the whole structure which can be seen as a reduced scale of a high energy barrier is shown in Figure 14.

Figure 14: Front view of the tested rockfall barrier prototype (by courtesy of national project C2ROP)

The barrier is formed by an ASM4 ring net which can slide along ten support cables: four upstream and downstream and two lateral. Because of the large span of the barrier, the wiring along the edges, presented in Figure 15, is complex. It is symmetric between the upstream and downstream edges. The two external cables link the lateral anchor with the head of the central post (cables A and A_{bis} drawn in blue in Figure 15) and two central cables connect the head of the first and third posts (cable B and B_{bis} drawn in red). Each cable holds partially the net and is free near the post's head. With this assembly, the net is hold by two cables in the centre of each modulus and by one cable near posts. Each supporting cable is anchored (either to the head of a post or to the cliff) by a device dissipating the energy which is usually called a brake. Their technology is often complex but most of the time their behaviour can be considered bi-linear elasto-plastic. The whole structure is anchored to the cliff at the base of the posts which are also held by three anchoring cables.

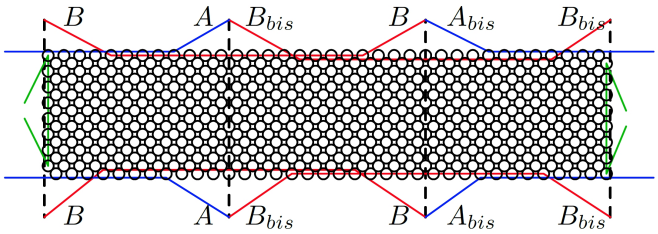

Figure 15: Detailed wiring between the net and the support cables

5.1.2. Quasi-static loading

A quasi-static loading is applied to the structure shown in Figure 14. A $740kg$ normalised polyhedral-shaped concrete block is held by a winch and slowly placed in the middle of the net until the barrier reaches equilibrium under dead-weight and block load. Then, another winch is hooked to the underside of the block and pulled perpendicularly to the net. Its vertical displacement is controlled and slowly increased so that the loading can be considered quasi-static. Several load cells are put on the fence supporting cables as well as on the winch. The whole resultant force applied to the structure and the tensile forces along some cables are thus recorded during the experiment.

5.2. Modelling of the barrier components and the loading

Beside the net, the other key components of the rockfall barrier are the support cables. They transfer the load applied to the net to the posts and the anchors. As explained in Section 5.1.1, they are connected with the posts and the anchors through brakes. When the net is impacted by a block, it slides along the support cables and concentrates around the impacted zone. This phenomenon, whose many modellings can be found in the literature [9, 35, 22, 6], is usually called the "curtain effect".

The characteristic behaviour of a brake is elasto-plastic and since a support cable is linked by one brake at each end, the set formed by the three elements has also a bi-linear elasto-plastic behaviour. For the modelling, the three elements (one cable with two brakes) are merged into one single element which is called "sliding cable" in the rest of this section. In the discrete modelling, a sliding cable represents a set of n ordered nodes which are linked to their neighbours by forces of same intensity [6]. The uniform tensile tension in the sliding cable is the consequence of the hypothesis that the contact points slide along it without friction. The idealised mechanical behaviour of the sliding cables is shown in Figure 16.

For the four upstream and downstream sliding cables, the values of the parameters introduced in Figure 16 are: $k_1 = 1140$ kN, $k_2 = 35$ kN, and $T_{lim} = 25$ kN, while for the two lateral sliding cables they are: $k_1 = 1190$ kN, $k_2 = 35$ kN, and $T_{lim} = 25$ kN. Those values are calibrated on separate experiments on brakes which were conducted in the framework of the national project C2ROP [29, 30].

Compared to the plane tensile test presented in Section 3.1, the net installed in the barrier is turned with an angle of $\frac{\pi}{4}$ (indeed one can see in Figure6 that the axes of the

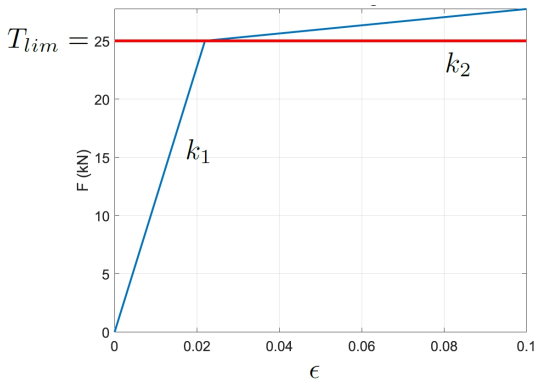

Figure 16: Numerical behaviour of the sliding cable elements

net periodic cell are rotated by $\frac{\pi}{4}$ relatively to the net unit axes). This change has little influence for models A and C but requires to modify locally the geometry of the rings linked to the edge cables in Model B, from square to triangle [similarly to 36, 10] (Figure 17). Using this new boundary rings, the strain limit theoretically increases according to the experiment conducted by H. Grassl. For simplicity, only the relaxed length of the modified ring was adjusted for the numerical computations.

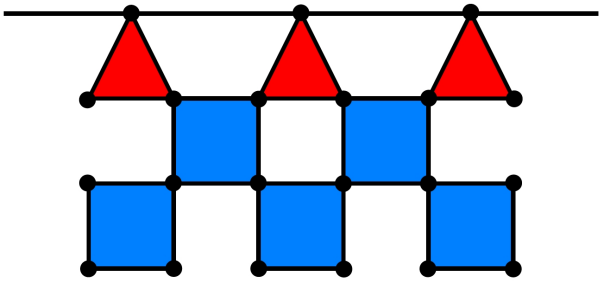

Figure 17: Triangular rings along the edge cable in Model B

Since the loading model is quasi-static, there is no risk of punching and the representation of the normalized block has very few influence on the whole structure behaviour. The block shape used for the numerical simulations is not polyhedral as in the experiment but spherical. Its diameter is 0.85 m and corresponds to the one of the sphere tangent to the edges of the polyhedron. Contact is modelled thanks to bar elements, which work only in compression and whose rest lengths correspond to the block radius. The nodes of the net slide hence without friction on the block. Their tensile stiffness is null while their behaviour is linear elastic in compression. The stiffness is determined according to the maximum tensile force applied to the structure and the tolerance of interpenetration. With a maximum force of almost 210kN and a tolerance of 1cm (which is in accordance with the accuracy induced by the discretisation as seen in section 4.2.2), the stiffness of the block bar is set to: $K_{block} = 5.10^6$kN/m. As in the physical experiment, the simulations are carried out by imposing the block displacement.

5.3. Comparison of the three models

5.3.1. Global barrier behaviour

The experimental force applied by the winch and the numerical behaviour calculated for each net model are presented in Figure 18. It is remarked that the overall behaviour in terms of force-displacement is well reproduced by the three net models. The modelling of the net seems to have little influence on the whole structure response (except may be for very large block displacements, where model A and B are stiffer).

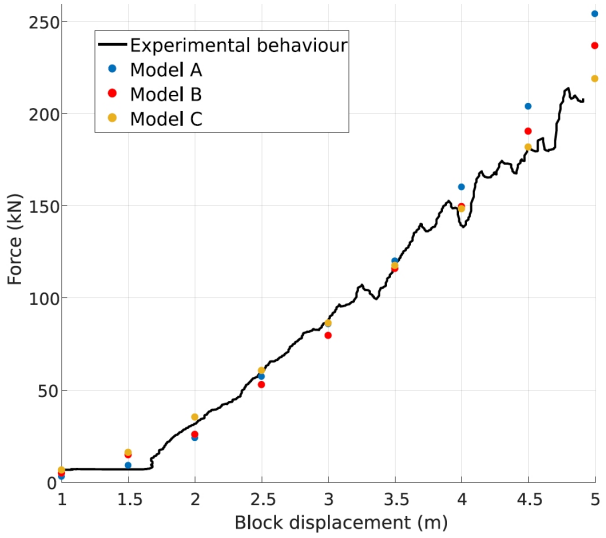

Figure 18: Comparison between the experiment and the three numerical force-displacement curves.

5.3.2. Resultant forces applied to the net boundary

After comparing the overall behaviour of the structure, the distribution of the forces applied along the boundary of the net is investigated. The forces applied by the net to the two lateral cables are not considered here because they are relatively low compared to that applied to the upper and lower cables. Furthermore, the force distributions along the upper and lower edges of the net are close due to the strong symmetry properties of the structure and the small displacements of the post heads. Only the one applied to the upper sliding cables is thus plotted in Figure 19. Five levels of the block vertical displacements are considered: from $1m$ to $5m$. The forces applied to the net boundary are plotted according to their application points along the edge.

Concerning the global behaviour, it is observed that, due to vertical deformation of the net and its sliding along its boundary, the loads tend to concentrate around the four points where the edge cables leave the net (see Figure 15). For a block displacement of $3m$ (Figure 19, graph (c)), the sliding of the net is almost achieved and the node distribution along the cable no longer changes. This load distribution is the same for the three models, and seems to depend only on the architecture of the fence.

However some differences in the intensity of forces between the three models can be noticed. During the first stage where the sliding occurs (graphs (a) and (b) of Figure 19), Model C concentrates forces in the central zone where deformations of rings are high and therefore where the net has become stiff. Model A presents low force everywhere, the lack of Poisson effect directs forces only to the supports points. Model B is uniformly stiff and therefore pulls everywhere on the edges. When the sliding is completely achieved (graphs (c), (d) and (e)), the behaviours of the three models become similar. The forces increases at the support points and more quickly at the two lateral points, located in $x = -4$ m and $x = 4$ m. However, the rates of force increase are different between the models and cor-

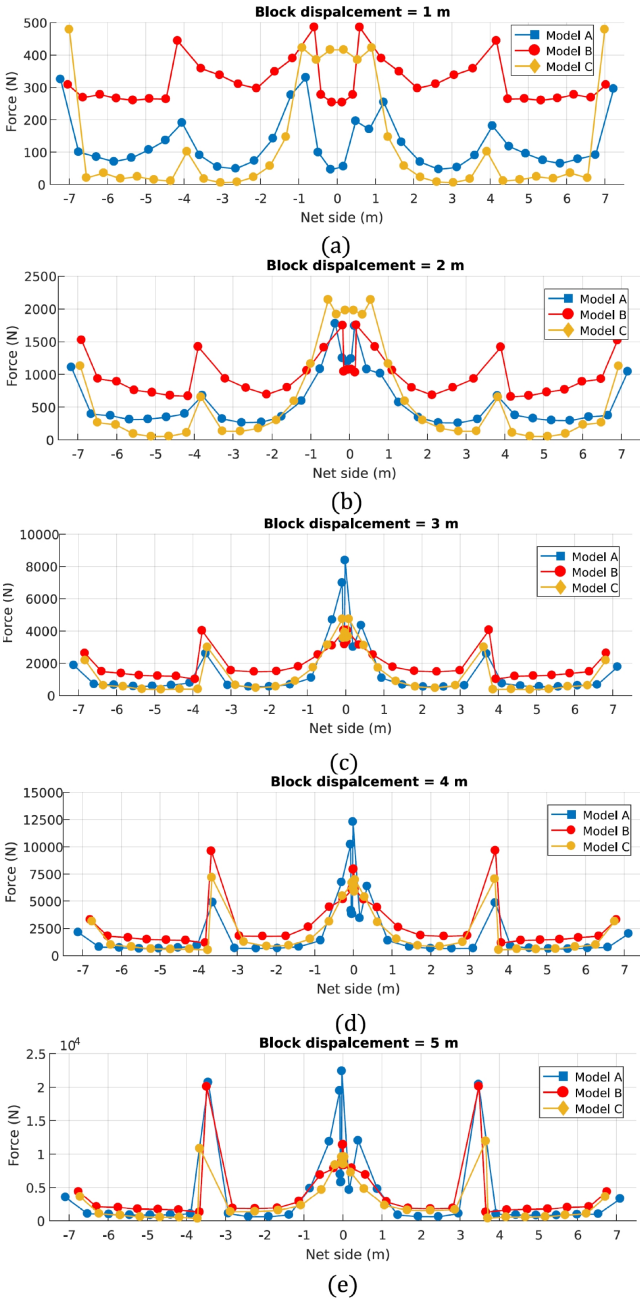

Figure 19: Force distribution on the upper edge of the net

related with their stiffness. Especially, the forces increase more quickly for Model A and B than for Model C.

5.3.3. Non-centred impacts

This last paragraph is devoted to the exploration of the states of equilibrium of the fence when the loading position changes in the plane of the net. For modelling simplicity, this time, perfect contacts between the block and the net are considered in this last section. Although very interesting from the designer point of view, direct interaction of the block with the posts is also neglected, the phenomena at stake would require a dedicated study which is too far from the scope of the present study. Indeed, the goal here is not to reproduce extreme loading cases in a realistic manner, but to study the influence of the net model on the behaviour of the structure. The loading is hence applied by imposing the position of the center of the block, which is here set to $3m$ in order to activate significantly the brakes (as observed in previous section).

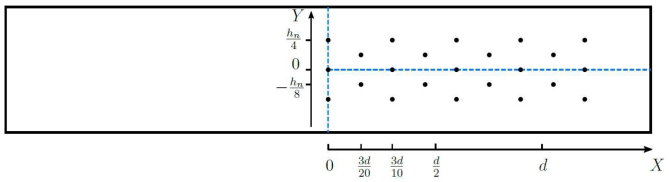

Figure 20: Position of the block used for the spatial characterisation of net behaviours.

The tested positions of the block in the plane of the net are presented in Figure 20, where the h_n and d indicate respectively the nominal height of the net and the dimension of a net unit. The centres of the modules are thus located at the abscissa $x = -d$, $x = 0$ and $x = d$ and the posts at abscissa $x = -3d/2$, $x = -d/2$, $x = d/2$ and $x = 3d/2$. As the radius of the block is between $h_n/8$ and $3d/20$, the positions of the block are limited to a band of height $h_n/2$ centred on the axis of symmetry of the net, to avoid local effect induced by direct interaction between the block and the edge cables. Then, considering symmetry of the modelled structure, the block positions are varied only on the right half of the net (see Figure 20). Afterwards, to facilitate the interpretation of the results, a continuous description of the properties is preferred and built using the natural neighbour interpolation of Matlab® on the entire strip. This interpolation being possible only between calculation points, results in following figures will be centered on the range $X \in \left[0; \frac{6d}{5}\right]$ $Y \in \left[-\frac{h}{4}; \frac{h}{4}\right]$.

The evolution of elastic deformation energy at equilibrium is shown in Figure 21. The distributions of the total strain energy are remarkably similar and cover a considerably large range from 50 kJ in the center to almost 200 kJ in the side module near an edge. For the three models, the strain energy increases towards the edges with a global minimum in the center and a local minimum near the center of the lateral units at the abscissa $x = 4.5m$. This local minimum is much more pronounced in model A than in models B and C. Considering that, in these simulations, the imposed height of the block is constant, the total strain energy is directly proportional to the force applied by the block on the net, and by there to the global stiffness of the structure. The areas with higher strain energy allow hence the identification of the areas where the stiffness of the barrier is higher. These areas correspond hence to the vicinity of the post and the lateral edge.

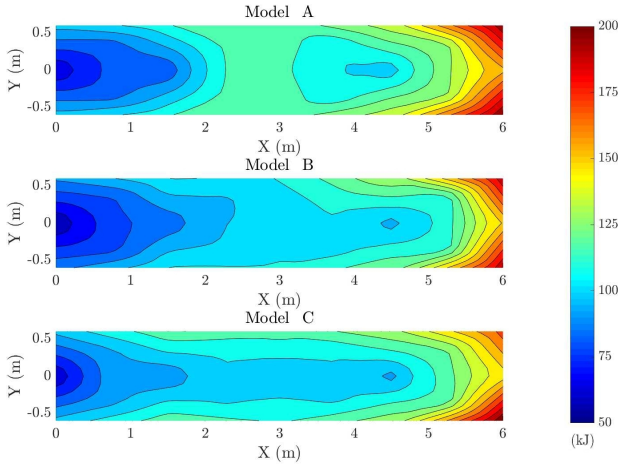

Figure 21: Evolution of the strain energy as a function of the block position for the three models.

Now that the influence of the position of the block on the total energy of the structure has been identified, the part of this energy which is due to the strain of the edge cables can be studied for each of the three models. The ratio of the strain energy stored in the cables and the total strain energy is hence shown in Figure 22. For the three models, at least 70% of the energy is stored in the edge cables (except in the central module of model C). The share of energy only due to the deformation of the edge cables seems thus to follow the evolution of the total energy: the structure is softer in the area where sliding is allowed (in the centre of the module) and solicit less the edge cables. To be more specific, the strain energy of edge cables splits into elastic and plastic energy dissipated by the brakes. Considering the high elastic stiffness of the cables and the low threshold of the brakes, it can be assumed that the strain energy in the edge cables approximates the energy dissipated by the brakes. Therefore, the higher the local stiffness of the net, the higher the share of the total energy dissipated by the brakes on the edge cables. Following this interpretation, model A is stiffer than model B which is also stiffer than model C (which apparently is in contradiction with observations made in section 4).

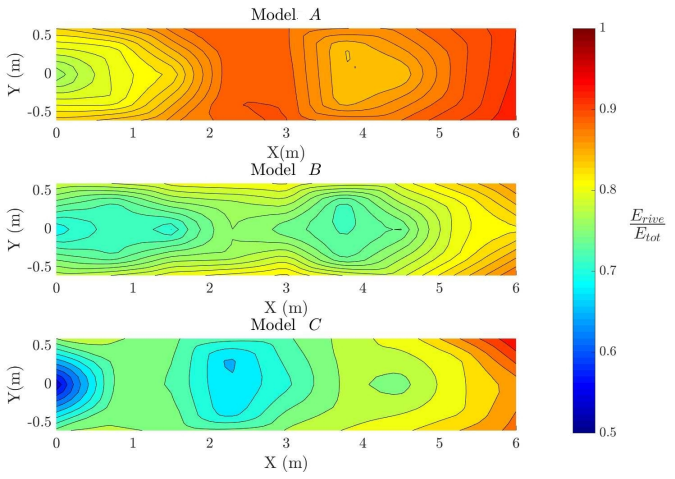

Figure 22: Evolution of the share of the strain energy stored in the edge cables as a function of the block position for the three models.

To explain this observation, one must go further into the comparison. To this end, the spread of the energy stored by the cables between the different cables has been analysed for the three models. It is chosen to focus on cable B_{inf} which runs from point B to point B on the bottom of figure 15, because it is the closest to the loaded area. Results of simulations are shown in Figure 23. The similarity of the three maps is remarkable. The maps relative to the other cables have also been plotted and show the same similarities. The maps for each cable being almost identical for the three models, it means that the split between the cables of the strain energy stored by each cable is similar and, by there that the load paths through the net to the anchor points is similar. Differences observed in Figure 22 must thus be attributed to differences in the energy stored by the nets.

We know from the first sections of this paper that the two asymptotic stiffnesses (flexural and tensile) of the models are all identical and calibrated on the same experiments. Their main difference relies in their ability to deform in the direction perpendicular to the principal strain (their ability to capture Poisson effect). Indeed, without Poisson effect, the net pulls straight forward to the hard points on its boundary (which correspond to the points where the edge cables leave the net). These points then slide until they almost joint. Afterwards, the net deforms only marginally and only the edge cables and the brakes concentrate the deformations. With Poisson effect, the forces toward hard points of the net go with perpendicular forces which encourage the rearrangement of the net and facilitate the sliding. By there, these forces give additional strain reserve in the loaded area and mobilise a larger part of the net which consequently store a larger part of the strain energy.

This analysis is confirmed by the study of the transverse height (the height measured perpendicularly to the cliff) which is the other key element of the European agreement. Transversal heights under loading are hence plotted in Figure 24 for the three models. Differences in the maps

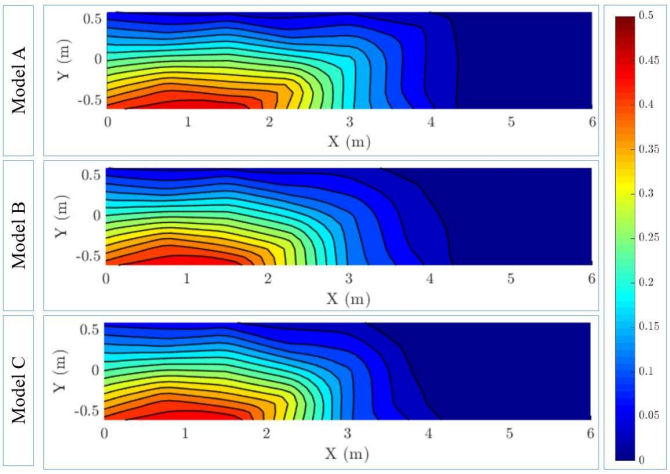

Figure 23: Evolution of the share of the strain energy stored in the cable B_{ing} as a function of the block position for the three models.

are significant and follow qualitatively the maps of the share of strain energy in the edge cables (see Figure 22). Poisson effect allows the spreading of strains in the net and consequently reduces deformation of the edge cables in the transverse direction.

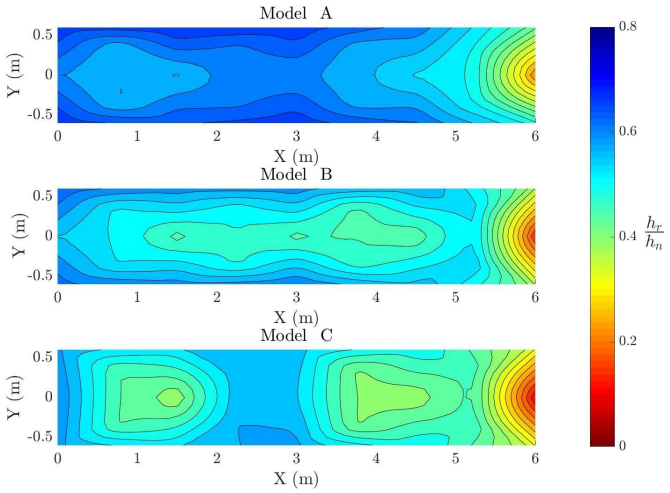

Figure 24: Evolution of the residual height as a function of the block position for the three models.

From this study on non-centered impacts, one can thus conclude that:

- the global behaviour of the barrier (Figure 14 and 21) as well as the load path through the net or the share of the energy dissipated by the brakes between the edge cables (Figure 23) are driven by the architecture of the barrier and not by the net model,
- the share on the energy stored by the net relatively to the total energy (Figure 21 as well as the residual height transversally to the loading direction (Figure 24) are linked with Poisson effect and therefore depend on the net model.

Depending hence on the objectives of the simulation, each of the three net models can be relevant and safely implemented by a designer. The authors would however recommend to use a model with Poisson effect, which means with ring interaction (i.e. model B or C), which can capture more aspects of the barrier behaviour.

6. Conclusion

In this paper, the influence of the discrete ring model in view of modelling the behaviour of ASM4 barriers was assessed. Three different modelling strategies have been compared. These strategies were adapted from existing models in the literature in order to built three typical characteristic modelling choice and to compare their consequence.

In the first stage, the intrinsic mechanical properties of the net models have been identified thanks to a robust homogenisation method, which allows to establish the expression of an equivalent elastic membrane tensors. This preliminary result gives an objective criterion to compare the behaviour of the discrete models and thus identify their intrinsic limitations. For instance, it has been deduced that the equivalent membrane of the spring model (model A) has a null Poisson ratio whereas that of the flexural ring model (model C) has a shear stiffness contrary to the others.

Then, using the form of the elasticity tensors, the mechanical property of the net models have been calibrated in such way that their axial stiffness was the same. The difficulty to reproduce the characteristic non-linear behaviour

of a ring was hence observed, as well as the different strategy to model it. A fictitious material non-linearity must be introduced for model A and B, while consistent geometric non linearities are naturally present in model C, so that calibration is only based on initial axial and bending stiffness.

The third stage of the comparison was dedicated to the study of a particular transformation, involving large space displacements and for which a closed form solution exists. This transformation has on one hand highlighted the advantage of the geometric non-linearity in model C, and on the other hand, allowed to validate the performance and the accuracy of the numerical tools.

Finally, the behaviours of the three models were studied on a whole rockfall barrier. All of them present remarkable agreement with the experimental results at global scale, despite the intrinsic difference in their local behaviour. This confirms hence one conclusion of Dugelas *et al* [15] who demonstrate that DEM models with different complexity level may result in similar abilities in predicting the barrier impact response. On the contrary, when looking at global deformations and residual height, the cable model (model A) was found much stiffer than the two others. This has been interpreted as a consequence of the nullity of the Poisson ratio which does not allow for a diffusion of the forces in both directions of the net and hence limits the rearrangement of the net around the loaded area.

This comparative assessment can further be used as guidelines for designers in order to chose their models, to interpret their results and to separate which aspect is intrinsecaly linked with the numerical model and which one is linked with the real structure behaviour.

Acknowledgements

The authors wish to thank all the members of the national project and particularly the members of the working group on flexible barriers for their invaluable support, namely M-A. Chanut and J. Coulibaly from CEREMA, P. Robit, I. Olmedo from GTS, C. Galandrin and M. Verdet from CAN, L. Dugelas form IRSTEA and D. Bertrand from INSA Lyon.

References

[1] A Cazzani, L Mongiovi, T. F. (2002). Dynamic finite element analysis of interceptive devices for falling rocks.pdf. *International Journal of Rock Mechanics and Mining Sciences 39*(3), 303–321.

[2] Adriaenssens, S. M. and M. R. Barnes (2001). Tensegrity spline beam and grid shell structures. *Engineering Structures 23*(1), 29–36.

[3] Bertrand, D., F. Nicot, P. Gotteland, and S. Lambert (2005). Modelling a geo-composite cell using discrete analysis. *Computers and Geotechnics 32*(8), 564–577.

[4] Bertrand, D., A. Trad, A. Limam, and C. Silvani (2012). Full-scale dynamic analysis of an innovative rockfall fence under impact using the discrete element method: From the local scale to the structure scale. *Rock Mechanics and Rock Engineering 45*(5), 885–900.

[5] Boulaud, R. (2020). *Etudes et modélisations du comportement d'un écran de filet pare-blocs à différentes échelles*. Ph. D. thesis, Université Paris Est.

[6] Boulaud, R., C. Douthe, and K. Sab (2020). Modelling of curtain effect in rockfall barrier with the dynamic relaxation. *International Journal of Solids and Structures*.

[7] Castanon-Jano, L., E. Blanco-Fernandez, D. Castro-Fresno, and D. Ferreño (2018). Use of explicit FEM models for the structural and parametrical analysis of rockfall protection barriers. *Engineering Structures 166*(March), 212–226.

[8] Coulibaly, J., M. Chanut, and S. e. a. Lambert (2019). Toward a generic computational approach for flexible rockfall barrier modeling. *Rock Mech Rock Eng 52*, 4475–4496.

[9] Coulibaly, J., M.-A. Chanut, S. Lambert, and F. Nicot (2018). Sliding cable modeling: An attempt at a unified formulation. *International Journal of Solids and Structures 130-131*, 1–10.

[10] Coulibaly, J. B., M.-A. Chanut, S. Lambert, and F. Nicot (2017). Nonlinear Discrete Mechanical Model of Steel Rings. *Journal of Engineering Mechanics 143*(9), 04017087.

[11] Day, A. (1965). An Introduction to Dynamic Relaxation. *the engineer*, 218–221.

[12] Dhakal, S., N. P. Bhandary, R. Yatabe, and N. Kinoshita (2011). Experimental, numerical and analytical modelling of a newly developed rockfall protective cable-net structure. *Natural Hazards and Earth System Science 11*(12), 3197–3212.

[13] Douthe, C. and O. Baverel (2009). Design of nexorades or recip-

rocal frame systems with the dynamic relaxation method. *Computers and Structures 87*(21-22), 1296–1307.

[14] Douthe, C., O. Baverel, and J. Caron (2006). Form-finding of a grid shell in composite materials. *Journal of the International Association for Shell and Spatial Structures 47*(150), 53–62.

[15] Dugelas, L., J. B. Coulibaly, F. Bourrier, S. Lambert, M.-A. Chanut, I. Olmedo, and F. Nicot (2019). Assessment of the predictive capabilities of discrete element models for flexible rockfall barriers. *International Journal of Impact Engineering 133*, 103365.

[16] Escallón, J. P., V. Boetticher, C. Wendeler, E. Chatzi, and P. Bartelt (2015). Mechanics of chain-link wire nets with loose connections. *Engineering Structures 101*, 68–87.

[17] Escallón, J. P., C. Wendeler, E. Chatzi, and P. Bartelt (2014). Parameter identification of rockfall protection barrier components through an inverse formulation. *Engineering Structures 77*, 1–16.

[18] Flanagan, D. P. and T. Belystrschiko (1981). A uniform strain hexahedron and quadrilateral with orthogonal hourglass control. *International Journal for Numerical Methods in Engineering 17*(1), 679–706.

[19] Florence, C. and K. Sab (2006). A rigorous homogenization method for the determination of the overall ultimate strength of periodic discrete media and an application to general hexagonal lattices of beams. *European Journal of Mechanics, A/Solids 25*(1), 72–97.

[20] Gentilini, C., G. Gottardi, L. Govoni, A. Mentani, and F. Ubertini (2013). Design of falling rock protection barriers using numerical models. *Engineering Structures 50*, 96–106.

[21] Gentilini, C., L. Govoni, S. de Miranda, G. Gottardi, and F. Ubertini (2012). Three-dimensional numerical modelling of falling rock protection barriers. *Computers and Geotechnics 44*, 58–72.

[22] Ghoussoub, L. (2015). *Analyse de quelques éléments du comportement des écrans de filets pare-blocs*. Ph. D. thesis, Université Paris Est.

[23] Grassl, H., A. Volkwein, E. Anderheggen, and W. J. Ammann (2002). Steel-net rockfall protection: Experimental and numerical simulation. *Structures under Shock and Impact VII*, 143–153.

[24] Mentani, A., L. Govoni, A. Giacomini, G. Gottardi, and O. Buzzi (2018). An equivalent continuum approach to efficiently model the response of steel wire meshes to rockfall impacts. *Rock Mechanics and Rock Engineering 0*(0), 0.

[25] Mentani, A., L. Govoni, G. Gottardi, S. Lambert, F. Bourrier, and D. Toe (2016). A New Approach to Evaluate the Effectiveness of Rockfall Barriers. *Procedia Engineering 158*, 398–403.

[26] Nicot, F. (1999). *Etude du comportement mécanique des ouvrages souples fr protection contre les éboulements rocheux*. Ph. D. thesis, Centrale Lyon.

[27] Nicot, F., B. Cambou, and G. Mazzoleni (2001). Design of rockfall restraining nets from a discrete element modelling. *Rock Mechanics and Rock Engineering 34*(2), 99–118.

[28] Olmedo, I., M.-A. Chanut, C. Douthe, M. Verdet, C. Galandrin, L. Dugelas, and D. Bertrand (2020). Etude experimentale multi-echelle sur les ecrans pare-blocs: comportement des ouvrages hors cadre etag27. *Revue Francaise de Geotechnique*.

[29] Olmedo, I., P. Robit, D. Bertrand, C. Galandrin, J. Coulibaly, and C. M-A. (2017). Extended experimental studies on rockfall flexible fences. In *Proceedings of Rocexs 2017 Barcelona Spain*.

[30] Olmedo, Ignacio, Chanut, Marie-Aurélie, Douthe, Cyril, Verdet, Mathieu, Galandrin, Clément, Dugelas, Loic, and Bertrand, David (2020). étude expérimentale multi-échelle sur les écrans pare-blocsomportement des ouvrages hors cadre etag27. *Rev. Fr. Geotech.* (163), 8.

[31] Peloux, L. D. (2018). *Modeling of bending-torsion couplings in active-bending structures. Application to the design of elastic gridshells*. Ph. D. thesis, Paris-Est.

[32] Sasiharan, N., B. Muhunthan, T. C. Badger, S. Shu, and D. M. Carradine (2006). Numerical analysis of the performance of wire mesh and cable net rockfall protection systems. *Engineering Geology 88*(1-2), 121–132.

[33] Thoeni, K., C. Lambert, A. Giacomini, and S. W. Sloan (2013). Discrete modelling of hexagonal wire meshes with a stochastically distorted contact model. *Computers and Geotechnics 49*, 158–169.

[34] Veenendaal, D. and P. Block (2012). An overview and comparison of structural form finding methods for general networks. *International Journal of Solids and Structures 49*(26), 3741–3753.

[35] Volkwein, A. (2004). *Numerische Simulation von flexiblen Steinschlagschutzsystemen*. Ph. D. thesis, ETH.

[36] Volkwein, A., L. Melis, B. Haller, and R. Pfeifer (2005). Protection from Landslides and High Speed Rockfall Events: Reconstruction of Chapman's Peak Drive. *IABSE Symposium Report 90*(6), 47–54.

[37] Volkwein, A., K. Schellenberg, V. Labiouse, F. Agliardi, F. Berger, F. Bourrier, L. K. Dorren, W. Gerber, and M. Jaboyedoff (2011). Rockfall characterisation and structural protection - A review. *Natural Hazards and Earth System Science 11*(9), 2617–2651.

[38] von Kármán, T. (1910). Festigkeitsproblem im Maschinenbau.